Yun *et al. Cell Communication and Signaling* (2024) 22:452
https://doi.org/10.1186/s12964-024-01810-8

Cell Communication and Signaling

RESEARCH Open Access

Non-thermal atmospheric pressure plasma induces selective cancer cell apoptosis by modulating redox homeostasis

Ju Hyun Yun[1], Yoon Hee Yang[2], Chang Hak Han[3], Sung Un Kang[3*†] and Chul-Ho Kim[3*†]

Abstract

Background Anticancer treatments aim to selectively target cancer cells without harming normal cells. While non-thermal atmospheric pressure plasma (NTAPP) has shown anticancer potential across various studies, the mechanisms behind its selective action on cancer cells remain inadequately understood. This study explores the mechanism of NTAPP-induced selective cell death and assesses its application in cancer therapy.

Methods We treated HT1080 fibrosarcoma cells with NTAPP and assessed the intracellular levels of mitochondria-derived reactive oxygen species (ROS), mitochondrial function, and cell death mechanisms. We employed N-acetylcysteine to investigate ROS's role in NTAPP-induced cell death. Additionally, single-cell RNA sequencing was used to compare gene expression in NTAPP-treated HT1080 cells and human normal fibroblasts (NF). Western blotting and immunofluorescence staining examined the expression and nuclear translocation of nuclear factor erythroid 2-related factor 2 (NRF2), a key antioxidant gene transcription factor. We also evaluated autophagy activity through fluorescence staining and transmission electron microscopy.

Results NTAPP treatment increased ROS levels and induced mitochondrial dysfunction, leading to apoptosis in HT1080 cells. The involvement of ROS in selective cancer cell death was confirmed by N-acetylcysteine treatment. Distinct gene expression patterns were observed between NTAPP-treated NF and HT1080 cells, with NF showing upregulated antioxidant gene expression. Notably, NRF2 expression and nuclear translocation increased in NF but not in HT1080 cells. Furthermore, autophagy activity was significantly higher in normal cells compared to cancer cells.

Conclusions Our study demonstrates that NTAPP induces selective cell death in fibrosarcoma cells through the downregulation of the NRF2-induced ROS scavenger system and inhibition of autophagy. These findings suggest NTAPP's potential as a cancer therapy that minimizes damage to normal cells while effectively targeting cancer cells.

Keywords Non-thermal atmospheric pressure plasma, Reactive oxygen species, NRF2, Autophagy, Fibrosarcoma

†Sung Un Kang and Chul-Ho Kim contributed equally to this work.

*Correspondence:
Sung Un Kang
cows79@ajou.ac.kr
Chul-Ho Kim
ostium@ajou.ac.kr

[1]Department of Otorhinolaryngology-Head and Neck Surgery, College of Medicine, Ewha Womans University, Seoul, Korea07985
[2]Department of Biomedical Sciences, Graduate School of Medicine, Ajou University, Suwon, Korea 16499
[3]Department of Otolaryngology, School of Medicine, Ajou University, Suwon, Korea16499

© The Author(s) 2024. **Open Access** This article is licensed under a Creative Commons Attribution-NonCommercial-NoDerivatives 4.0 International License, which permits any non-commercial use, sharing, distribution and reproduction in any medium or format, as long as you give appropriate credit to the original author(s) and the source, provide a link to the Creative Commons licence, and indicate if you modified the licensed material. You do not have permission under this licence to share adapted material derived from this article or parts of it. The images or other third party material in this article are included in the article's Creative Commons licence, unless indicated otherwise in a credit line to the material. If material is not included in the article's Creative Commons licence and your intended use is not permitted by statutory regulation or exceeds the permitted use, you will need to obtain permission directly from the copyright holder. To view a copy of this licence, visit http://creativecommons.org/licenses/by-nc-nd/4.0/.

Background

Cancer presents a significant global health challenge, and while chemotherapy and radiotherapy serve as primary treatment modalities, they come with various complications and side effects [1]. These treatments not only target cancer cells but also inflict harm on normal cells, resulting in complications such as fatigue, chronic pain, and organ toxicity [2, 3]. While these treatments have contributed to increased life expectancy, cancer survivors may experience prolonged toxicity. Hence, there is an urgent need for the development of novel anticancer agents capable of selectively targeting cancer cells while preserving normal ones, thus enhancing patient quality of life.

Plasma has recently emerged as a promising next-generation therapeutic agent. Plasma forms when energy is applied to a gas and can be obtained as non-thermal atmospheric pressure plasma (NTAPP) under atmospheric pressure at temperatures below 40 °C [4, 5]. Moreover, since plasma does not cause thermal damage to tissues, its potential applications across various medical domains, including antiseptics, skin wound healing, tooth bleaching, and cancer therapy, have been extensively explored [6–12].

Plasma exhibits a selective anticancer effect due to the differential basal levels of reactive oxygen species (ROS) between normal and cancer cells. Cancer cells typically generate higher levels of ROS than normal cells, resulting in hyperactivation of cellular signaling pathways crucial for maintaining cellular transformation and cancer progression [13]. Despite cancer cells' upregulated antioxidant processes and altered redox equilibrium, a critical threshold of ROS can trigger cancer cell death through various mechanisms [14–16]. Notably, elevated intracellular ROS levels can induce apoptosis in cancer cells by causing cell membrane breakdown and damage, as evidenced by previous studies involving mouse tumor models [17, 18].

In this study, our objective was to elucidate the disparate effects of NTAPP on fibroblasts and fibrosarcoma cells and to investigate the specific mechanisms through which NTAPP induces selective cell death.

Materials and methods

Experimental design of plasma-treated solution (PTS) treatment

A plasma-treated solution (PTS) was prepared using oxygen and helium gas [18], employing a NTAPP system (Fig. S1a and b). The system featured two electrodes crafted from Al_2O_3, with dimensions of 10×40 mm^2 for the ground electrodes, an inter-electrode gap of 2 mm, a power range of approximately 2–13 kV, and an average frequency of approximately 20–30 kHz. Plasma treatment was administered at a rate of 1 min/mL, with the distance between the plasma nozzle and the culture media maintained at approximately 1 cm. Following treatment, the medium's temperature remained unchanged, and pH values were measured at 7.8–8.2, 8.3, and 8.3 for helium + oxygen, nitrogen, and nitrogen + argon, respectively, as carrier gases (Fig. S1c).

Cell lines and reagents

The human fibrosarcoma cell line HT1080 was procured from the Korean Cell Bank (Seoul, Korea), while the FaDu and HaCaT cell lines and primary dermal fibroblasts (HDFa, PCS-201-012) were purchased from the American Type Culture Collection (Manassas, VA, USA). HT1080 cells were cultured in Roswell Park Memorial Institute-1640 medium (Gibco, Carlsbad, CA, USA), FaDu cells in minimum essential medium (Gibco), and HDFa and HaCaT cells in Dulbecco's Modified Eagle's medium (Gibco). The culture media were supplemented with 10% fetal bovine serum and penicillin-streptomycin (100 U/ml, Gibco) and maintained at 37 °C with 5% CO_2 under humidified conditions. HDFa cells between passages 6 and 9 were utilized for analyses. N-acetylcysteine (NAC) was procured from Sigma-Aldrich (St. Louis, MO, USA).

Dead/live cell assay

Dead/live cell viability/cytotoxicity assays were conducted utilizing calcein acetoxymethyl ester and ethidium homodimer-1, both sourced from Thermo Fisher Scientific (Rochester, NY, USA) [19]. In brief, cells were seeded into 12-well culture plates at a density of 2×10^3 cells/well, and the impact of PTS treatment on cell viability was assessed 24 h post-treatment. Fluorescent images were acquired using the EVOS FL Auto Cell Imaging System (Thermo Fisher Scientific).

Fluorescence-activated cell sorting (FACS) analysis (annexin V–PI staining)

Apoptotic cell death was identified utilizing the FITC Annexin V-PE Apoptosis Detection Kit I, following the manufacturer's protocol (556547, BD Biosciences, Bedford, MA, USA), as previously outlined [18]. The distribution of apoptotic cells per 10,000 cells was determined using a BD FACS Aria III instrument (BD Biosciences), with excitation and emission wavelengths set at 488 and 530 nm, respectively.

Terminal deoxynucleotidyl transferase dUTP nick end labeling (TUNEL) analysis

DNA fragmentation resulting from apoptosis was assessed using an in-situ cell death detection kit (11684795910, Roche Molecular Biochemicals, Basel, Switzerland), as described previously [18]. Fluorescent images of apoptotic cells were captured randomly using a

fluorescence EVOS FL Auto microscope (Thermo Fisher Scientific).

Western blot analysis

Western blot analysis was conducted following established protocols [18]. In brief, cells were lysed using Radioimmunoprecipitation assay (RIPA) buffer (R0278, Sigma-Aldrich), with the addition of 1× protease inhibitor cocktail and 1× PhoSTOP (Roche Molecular Biochemicals). Primary and secondary antibodies (anti-rabbit IgG [#7074] or anti-mouse IgG [#7076]; dilution 1:2000) were procured from Cell Signaling Technology (Danvers, MA, USA), while the OXPHOS cocktail (ab110411) was purchased from Abcam (ab117600, Cambridge, UK). Immunoreactive proteins were detected using an ECL western blot analysis kit (RPN2235, GE Healthcare, Chicago, IL, USA), and results were analyzed using the ImageQuant™ LAS 4000 (GE Healthcare).

Measurement of mitochondrial superoxide localization and ROS generation

To quantify ROS and mitochondrial superoxide production, cells were treated with PTS for 24 h, followed by treatment with 10 μM hydroethidine (HE, D1137 Molecular Probes, Eugene, OR, USA) and MitoSOX Red (M36008, Molecular Probes) [20]. Fluorescence-stained cells (1×10^4) were analyzed using FACS. Additionally, to examine mitochondrial superoxide localization, cells on coverslips were exposed to 2.5 mM MitoSOX Red for 10 min, followed by staining with 180 nM MitoTracker Green (M7514, Molecular Probes) for 20 min at 37 °C. Images were captured and processed using an EVOS FL Auto fluorescence microscope (Thermo Fisher Scientific).

Mitochondrial membrane potential (MMP) assay

MMP was assessed using FACS with the FACS Aria III system (BD Biosciences) and fluorescence microscopy (EVOS Auto) utilizing the JC-1 system (T3168, lipophilic cationic probe 5,5,6,6-tetrachloro-1,1,3,3-tetra ethylbenzimidazolcarbocyanine iodide; Molecular Probes) [20].

RNA sequencing, identification of differentially expressed genes (DEGs), and gene ontology (GO) analysis

RNA sequencing was conducted following established protocols [21]. Total RNA was extracted from the cells and subjected to next-generation sequencing (NGS) at DNA Link Incorporation (Seodaemun-Gu, Seoul, Korea). Sequence reads underwent processing using the Tuxedo Suite (Baltimore, MD, USA), and aligned reads were assembled using Cufflinks software version 2.0.2 to predict transcript structures and compare transcriptome profiles based on the RNA-Seq data. Gene expression levels in the non-side population (NSP) were utilized as control data to determine the up- or downregulation of gene expression in the side population (SP) cells. Genes with a p-value < 0.05 and log2-transformed values <−1 or >1 were considered statistically significant DEGs. Heatmaps were generated based on the DEG data ($N=3$).

Real-time quantitative PCR (qPCR) assay

Real-time PCR assays were conducted following established procedures [21]. Target genes were quantified via one-step real-time PCR using StepOnePlus™ (Applied Biosystems, Foster City, CA, USA). PCR primers were procured from Qiagen (Hilden, Germany), and *GAPDH* mRNA levels were utilized for normalization.

Isolation of nuclear and cytoplasmic extracts

Nuclear and cytoplasmic protein fractionation was performed following previously described methods [22]. Nuclear and cellular extracts were isolated from vehicle cells or cells treated with PTS for 24 h using the NE-PER Nuclear and Cytoplasmic Extraction Reagent Kit (78833, Thermo Fisher Scientific) in accordance with the manufacturer's instructions.

Immunocytochemical analyses

Immunocytochemical assays were conducted following established protocols [21]. SP cells were cultured on microscope coverslips (Thermo Fisher Scientific) and treated with PTS. After 24 h, the coverslips were washed with 1× PBS and fixed in 4% paraformaldehyde for 15 min. Subsequently, blocking was performed for 1 h using bovine serum albumin (in 5% PBST). The slides were then incubated with primary antibodies (NRF2, LC3B) (1:200; Cell Signaling Technology) for 2 h, followed by PBS washes and incubation with Alexa 488-labeled antibodies (1:250; Thermo Fisher Scientific) for 1 h. Hoechst 33,258 and rhodamine phalloidin (1:50; R415, Thermo Fisher Scientific) were applied for 15 min to counterstain nuclei and F-actin, respectively. After PBS washes, the slides were mounted with VECTASHIELD (Vector Laboratories, Inc., Burlingame, CA, USA, H-1000) and examined using a confocal microscope (LSM 710, Carl Zeiss, Germany) and fluorescence microscopy (EVOS FL auto, Thermo Fisher Scientific).

Transmission electron microscopy (TEM)

Cells were fixed in 2% glutaraldehyde following 24 h of PTS treatment [21]. Subsequently, all sections were observed using an electron microscope (JEM-1011 JEOL, Tokyo, Japan) at an acceleration voltage of 80 kV. The images obtained were analyzed utilizing the Megaview III Soft imaging system (Olympus Soft Imaging Solution GmbH, Münster, Germany).

RNAi transfection

Transient siRNA transfection (Cell Signaling Technology) was executed using Lipofectamine™ RNAi/MAX reagent (13778100, Thermo Fisher Scientific) [21].

Measurement of extracellular ROS and nitric oxide

Extracellular ROS production was measured by treating the cell supernatant with Amplex Red assay reagent (Invitrogen, Carlsbad, CA, USA) and incubating it at 20–25 °C for 30 min. Nitric oxide production was determined by assessing stable nitrite levels using Griess reagent (Abcam), following the manufacturer's protocol. Briefly, 50 µl of the supernatant was added to a 96-well plate, followed by the addition of 50 µl sulfanilamide and 50 µl N-1-naphthylethylenediamine dihydrochloride. The concentrations of hydrogen peroxide and nitric oxide in the supernatant were then measured using a microplate reader (Epoch 2, BioTek Instruments Inc., Winooski, VT, USA) with excitation set at 540 nm. NO_3^- level was determined using a Colorimetric Nitric Oxide Assay Kit (ab65328, Abcam) and detected using an EPOCH microplate reader (BioTek).

Cell viability

Cell viability assays were conducted as previously outlined [21]. The optical density of each culture well was measured using an EPOCH microplate reader (BioTek) at 540 nm. Cells were seeded into 96-well cell culture plates at a density of 2×10^3 cells/well. Following 24 h, the cells were treated with PTS and assessed thereafter. Cell viability was expressed as ratios relative to the viability of untreated cells.

GFP-LC3 transfection

An assay using the pEGFP-LC3 plasmid was performed to assess autophagy as previously reported [23]. pEGFP-LC3 was a gift from Tamotsu Yoshimori (Addgene plasmid #21073) [24]. Transfection with the pEGFP-LC3 was carried out using Lipofectamin 2000 reagent (Thermo Fisher Scientific, MA, USA) and fluorescence microscopic images were captured at 7 and 24 h after the addition of PTS.

Statistical analysis

All statistical analyses were conducted using SPSS software ver29.0 (SPSS, Chicago, IL, USA). Data were presented as the mean±standard deviation. Statistically significant differences between groups in each assay were determined using the Mann–Whitney U test, one-way analysis of variance, Tukey's test, and the least significant difference post hoc test. Differences were considered statistically significant at $p<0.05$.

Results

Selective apoptotic effect of PTS on cancer cells

PTS demonstrates a selective induction of apoptosis in various tumor cells while sparing normal cells [18]. Notably, PTS significantly decreased cell viability in the two cancer cell lines (HT1080 and FaDu) but exhibited no impact on the two normal cell lines (NF and HaCaT) (Fig. 1a and b). Moreover, a distinct reduction in the viability of lung and thyroid cancer cells was evident following PTS treatment (Fig. S2a). Longitudinal assessment of cell viability further revealed a time-dependent decline solely in the cancer cells used. Conversely, nitrogen-based gas plasma treatment showed no effect on cell viability (Fig. S3).

PTS treatment markedly elevated the population of Annexin V/PI double-positive cancer cells exclusively, corroborating the cancer cell-specific apoptotic response (Fig. 1c, Fig. S2b). Additionally, examination of cellular morphology unveiled typical apoptotic features in the cancer cells used subsequent to PTS treatment (Fig. S4). Western blot analysis further unveiled heightened expression of apoptosis-related markers, including poly (ADP-ribose) polymerases (PARP) and cleaved caspase 3, alongside key signaling molecules implicated in cell death (p-ERK, p-JNK, and p-p38), solely in PTS-treated cancer cells (Fig. 1d). Furthermore, exclusive TUNEL-positive staining was observed in PTS-treated cancer cells (Fig. 1e).

PTS-induced mitochondrial damage selectively triggers cancer cell death by regulating ROS levels and MMP

Our prior investigations have demonstrated that NTAPP induces apoptosis in cancer cells through the accumulation of intracellular ROS originating from the mitochondria, resulting in the disruption of the MMP [18]. Upon PTS treatment, two cancer cell lines exhibited significant increases in ROS levels (Fig. 2a, Fig. S2c). Microscopic examination revealed co-localization of the MitoSOX-stained area (indicative of ROS, red) and Mitotracker-stained spots (representing mitochondria, green) within these cell lines. Additionally, flow cytometry analysis (FACS) demonstrated heightened mitochondrial superoxide levels subsequent to PTS treatment (Fig. 2b). Furthermore, PTS treatment led to a selective increase in MMP ($\Delta\Psi m$, indicated by green fluorescence) solely within the two cancer cell lines, signifying mitochondrial damage and MMP loss as evidenced by JC-1 staining (Fig. 2c). Notably, PTS treatment downregulated the expression of various mitochondrial proteins, particularly impacting mitochondrial metabolic proteins such as pyruvate dehydrogenase and OXPHOS I (Fig. 2d). These findings collectively suggest that PTS-induced apoptosis in cancer cells is facilitated by ROS accumulation resulting from mitochondrial dysfunction.

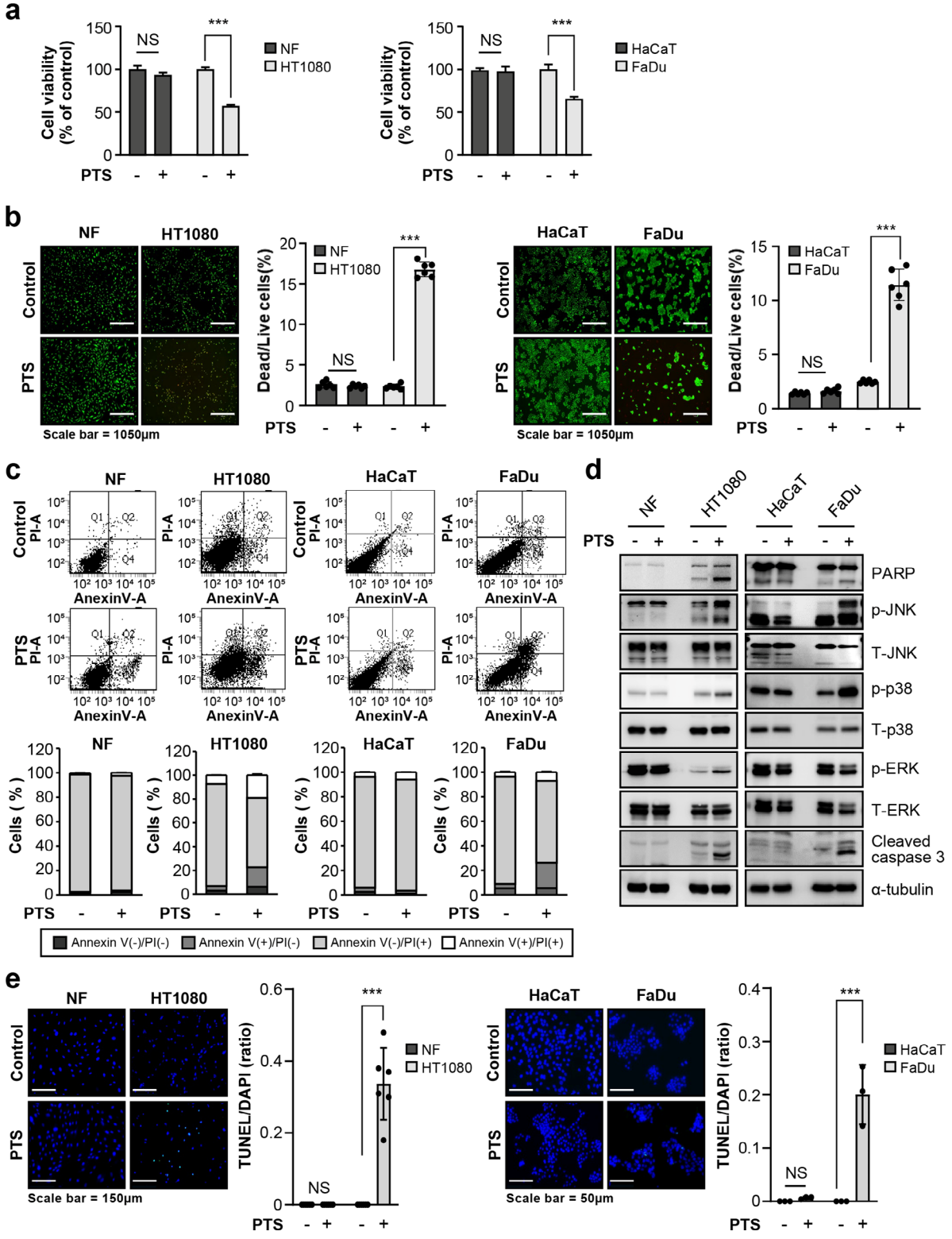

Fig. 1 Induction of selective apoptosis in cancer cells following plasma-treated solution (PTS) treatment. Human normal fibroblasts (NF), human fibrosarcoma (HT1080), human keratinocytes (HaCaT), and hypopharyngeal cell carcinoma (FaDu) cells were analyzed 24 h after PTS treatment (sec/ml). (**a**) Cell viability assay. (**b**) Dead/live cell viability and cytotoxicity assays. Cells were visualized using fluorescence imaging. Scale bar: 1050 μm. (**c**) Apoptosis analysis results obtained using fluorescence-activated cell sorting (FACS) and Annexin-VI staining. (**d**) Western blot analysis results obtained using antibodies against PARP, cleaved caspase-3, p-ERK, p-JNK, and p-p38. (**e**) Terminal deoxynucleotidyl transferase dUTP nick end labeling (TUNEL) assay. Fluorescence images of apoptotic cells were obtained using a fluorescence microscope. Scale bar: 50, 150 μm. NS: not significant; $^{*}p < 0.05$; $^{***}p < 0.001$

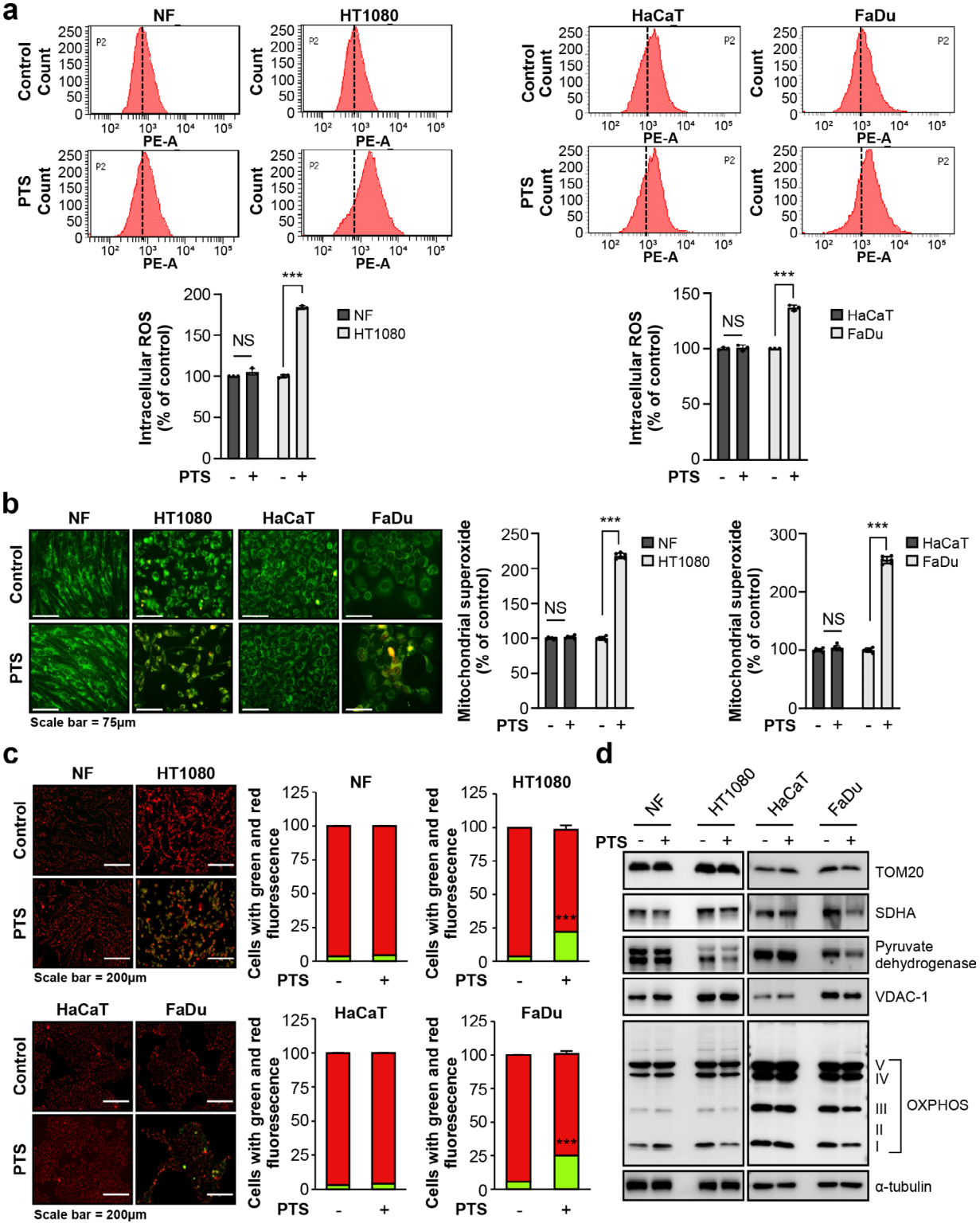

Fig. 2 Plasma treated solution (PTS)-induced apoptosis in cancer cells via the upregulation of mitochondrial reactive oxygen species (ROS) and mitochondrial dysfunction. NF, HT1080, HaCaT, and FaDu cells were treated with PTS for 24 h, followed by the addition of 10 μM hydroethidine and MitoSOX Red. (**a**) Fluorescence-stained cells were analyzed using fluorescence-activated cell sorting (FACS) to evaluate intracellular ROS levels. (**b**) Cells were exposed to MitoTracker Green for 20 min to localize mitochondrial superoxide radicals (red: Mito-SOX stained area, ROS; green: Mitotracker-stained area, mitochondria). Scale bar: 75 μm. (**c**) Mitochondrial membrane potential was evaluated via JC-1 staining. Scale bar: 200 μm. (**d**) Western blot analysis results showing decreased expression of pyruvate dehydrogenase and OXPHOS, particularly OXPHOS complex I. NS: not significant; ***$p < 0.001$

Inactivation of mitochondria-derived ROS and cancer cell apoptosis by ROS scavenger

To ascertain whether apoptotic cell death signaling was initiated by ROS, we conducted loss-of-function tests using NAC, a well-established ROS scavenger. Dead/live cell assays conducted with NAC demonstrated significant inhibition of PTS-induced cancer cell death (Fig. 3a), further validated by Annexin V-PI analysis (Fig. 3b). NAC effectively prevented the substantial increase in ROS production induced by PTS (Fig. 3c). Similarly, the impact of NAC was evident through the reduction in co-localized areas of MitoSOX and MitoTracker. FACS data supported these findings, showing NAC's ability to attenuate PTS-induced mitochondrial superoxide production (Fig. 3d). Furthermore, NAC treatment reversed PTS-induced changes in MMP in the cancer cells used (Fig. 3e). However, no significant alterations in ROS generation were observed in the normal cells used following PTS or NAC treatment. The overall increase in the expression levels of cytosolic PARP and cleaved caspase-3 induced by PTS treatment was notably reduced with co-treatment of NAC and PTS (Fig. 3f).

PTS-induced selective cancer cell death accompanied by upregulation of NRF2-mediated defense response in normal cells

Cancer cells exhibit heightened vulnerability to PTS-induced oxidative stress due to their inherently elevated ROS levels, resulting in an imbalanced redox status [25, 26]. Conversely, normal cells can regulate excessive intracellular ROS levels by upregulating antioxidant enzyme transcription. Therefore, to elucidate the genetic mechanisms contributing to the disparate responses of normal and cancer cells to PTS treatment, RNA sequencing was conducted. The expression levels of 969 genes were altered in PTS-treated cells more than two-fold compared to control cells (Fig. 4a). Furthermore, GO analysis of these 969 genes revealed their involvement in oxidative response and mitochondrial metabolism (Fig. 4b). A heat map in Fig. 4c illustrates nine genes associated with antioxidant enzymes and mitochondria-related genes in PTS-treated cells, consistent with the known regulation of ROS via inducible antioxidant programs, primarily through NRF2-Keap1 signaling [27]. qPCR analysis further confirmed significantly higher expression levels of *NRF2* genes in PTS-treated groups compared to control groups (Fig. 4d). No significant change in *NRF2* expression was observed in the cancer cells used; however, mitochondria-related genes were notably downregulated in these cells (Fig. 4a-d). Western blot analysis also validated increased expression of NRF2 and SOD1 in the normal cells used. Consistent with previous reports, a higher level of NRF2 was observed in non-treated HT1080 cells compared to NF cells (Fig. 4e) [28]. The nuclear translocation of NRF2 is closely associated with its transcriptional activity [29]. PTS-treated NF cells exhibited increased NRF2 protein levels in the nuclear fraction, whereas nuclear NRF2 expression was undetectable in HT1080 cells (Fig. 4f). Furthermore, confocal microscopy revealed notable NRF2 nuclear translocation in PTS-treated NF cells, while HT1080 cells showed no nuclear NRF2 localization (Fig. 4g). These findings suggest that PTS treatment not only upregulates the transcriptional level of NRF2 in normal cells but also enhances its nuclear localization, resulting in increased expression of antioxidant proteins.

NRF2 modulates ROS-dependent mitochondrial metabolic responses

Cell survival significantly decreased in both the NRF2 siRNA- and PTS-treated groups compared to the control siRNA group, exhibiting a consistent trend across the normal and cancer cells used (Fig. 5a). Furthermore, Annexin V-PI staining unveiled that NRF2 knockdown heightened sensitivity to PTS-induced apoptosis, with cancer cells particularly affected (Fig. 5b). Western blot analysis consistently demonstrated elevated PARP protein levels following PTS treatment in cells treated with NRF2 siRNA (Fig. 5c). Moreover, NRF2 knockdown led to a significant reduction in PTS-induced antioxidant protein (HO-1) expression in both cell lines (Fig. 5d). Levels of NRF2 in the cytoplasm and nuclei notably decreased in cells exhibiting downregulated NRF2 expression, with a significant suppression observed in nuclear protein levels across both cell types (Fig. 5e). Recent findings propose that mitochondrial ROS activates NRF2 [30]. NRF2 downregulation markedly increased PTS-induced mitochondrial superoxide generation in both cell lines, with cancer cells showing a particularly heightened response (Fig. 5f). Additionally, NRF2 downregulation significantly decreased levels of OXPHOS complex I (pyruvate and malate) post-PTS treatment, as observed via western blotting (Fig. 5g). Furthermore, NRF2 downregulation substantially augmented sensitivity to PTS-induced MMP reduction (Fig. 5h). These findings suggest a pivotal role for NRF2 in regulating PTS-induced mitochondrial redox processes.

Autophagy regulates redox homeostasis via STSQM1/KEAP1 interaction

The findings from our prior investigation demonstrated that PTS induces ROS-related apoptosis in cancer cells [18]. Nonetheless, the mechanisms underlying apoptosis inhibition and redox maintenance in normal cells remain unclear. Recent literature has emphasized the role of STSQM1 (p62) in modulating NRF2 and redox homeostasis through direct interaction with Keap1 under ROS-induced stress. Therefore, we explored the relevance of

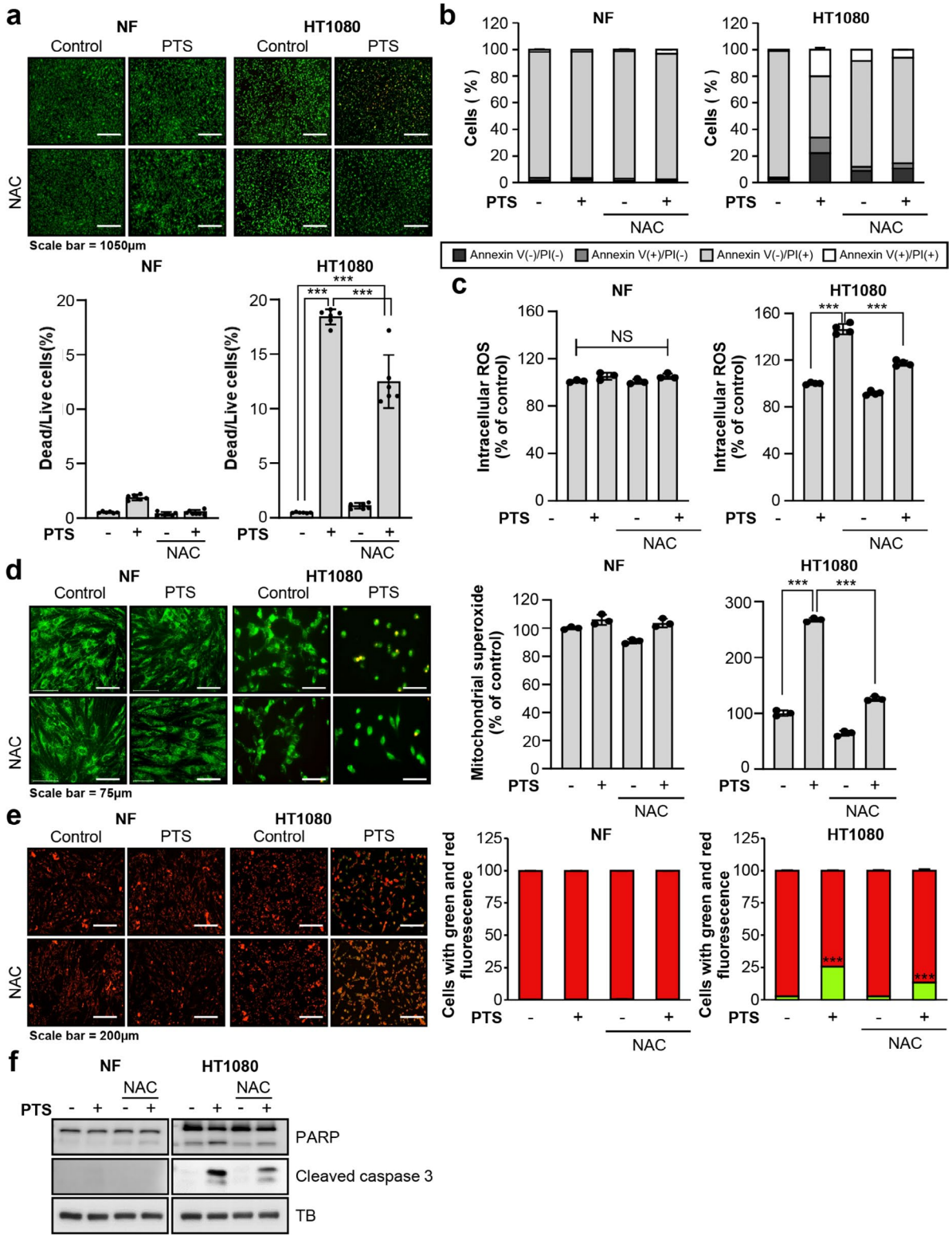

Fig. 3 Effect of a reactive oxygen species (ROS) scavenger on plasma treated solution (PTS)-induced mitochondria-derived ROS and apoptotic cell death in cancer cells. NF and HT1080 cells were treated with 10 mM N-acetylcysteine (NAC) for 1 h before PTS treatment. (**a**) Dead/live cell assays. Scale bar: 1050 μm. (**b**) Apoptotic cell death was measured using fluorescence-activated cell sorting and Annexin-VI staining. (**c**) Intracellular ROS generation was quantified using dihydroethidium staining. (**d**) Mitochondrial superoxide levels were measured using MitoSOX and MitoTracker kits. Scale bar: 75 μm. (**e**) Mitochondrial membrane potential was measured via JC-1 staining. Scale bar: 200 μm. (**f**) Western blot analysis results obtained using antibodies against PARP and cleaved caspase-3. NS: not significant; ***$p < 0.001$

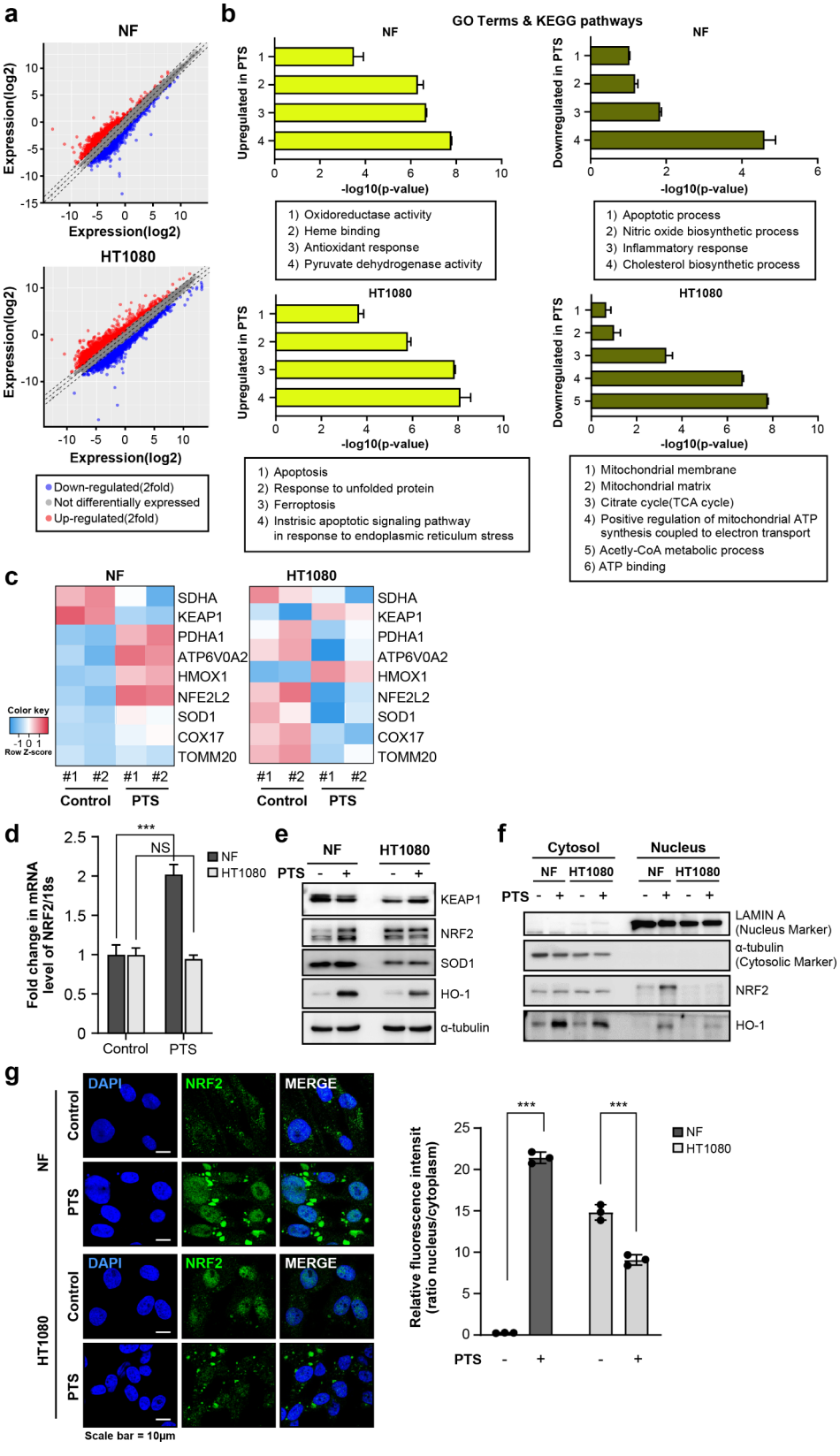

Fig. 4 (See legend on next page.)

(See figure on previous page.)

Fig. 4 Upregulated NRF2-mediated defense response in plasma treated solution (PTS)-treated normal cells. RNA sequencing was conducted to discern the differential gene expression patterns between PTS-treated and untreated NF and HT1080 cells. (**a**) Scatter plot illustrating global gene expression in PTS-treated NF and HT1080 cells compared to control cells, with genes represented by dots (red indicating upregulated genes, blue indicating downregulated genes). (**b**) Gene Ontology analysis of 969 regulated genes following PTS treatment. (**c**) Heatmap displaying RNA-Seq expression data depicting differentially regulated genes post-PTS treatment. (**d**) qPCR analysis revealing the expression of *NRF2* genes. (**e**) Western blot analysis results employing antibodies against Keap1, NRF2, HO-1, and SOD1. (**f**) Western blot analysis of subcellular fractionated nuclear and cytosolic lysates. (**g**) NRF2 immunostaining images of NF and HT1080 cells (blue: 4′,6-diamidino-2-phenylindole (DAPI); green: NRF2). The right panels depict merged images of NRF2 and DAPI, along with quantification of relative fluorescence intensity (nucleus/cytoplasm). Scale bar: 10 μm. NS: not significant; ***$p < 0.001$

PTS-induced NRF2 activation and autophagy in normal cells. We conducted an analysis of autophagy signaling at 7- and 24-hours following PTS treatment. The expression of ATG5 and ATG3 was increased at 7-hours post-PTS treatment. Also, PTS upregulated the expression of autophagy-specific markers, LC3B and p62. The LC3II/LC3I ratio indicates that autophagic flux is more strongly induced in NF cells than in HT 1080 cells (Fig. 6a, Fig. S5). It was confirmed that PTS activated autophagy through GFP-LC3 transfection in the normal cell used (Fig. 6b). This discovery was further supported by a notable increase in green puncta (LC3B) observed in PTS-treated normal and cancer cells (Fig. 6c). TEM analysis additionally confirmed PTS-induced autophagosome formation, particularly in NF cells (Fig. 6d). Figure 6e illustrates a significant augmentation in Keap1-p62 co-localization following PTS treatment, endorsing the notion of Keap1 degradation via autophagy. Knockdown of NRF2 in NF cells led to decreased levels of LC3B and p62 proteins compared to observations in control siRNA-treated NF cells. Conversely, in HT1080 cells, NRF2 knockdown did not decrease LC3B levels (Fig. 6f). Additionally using the autophagy inhibitor chloroquine, the association of autophagy with PTS treatment was confirmed (Fig. S6). These data reveal that autophagy is related to ROS homeostasis in NF cells.

Discussion

Fibrosarcoma, a rare and notably aggressive subtype within the spectrum of soft-tissue sarcomas, poses diagnostic challenges due to its nonspecific symptoms, often leading to diagnosis at an advanced stage [31]. The primary treatment for fibrosarcomas typically involves extensive surgical excision, with radiotherapy and chemotherapy commonly employed as neoadjuvant or adjuvant therapies [32]. However, the prognosis for fibrosarcomas remains bleak, primarily due to their low sensitivity and high recurrence rate, which limit the efficacy of traditional radiotherapy and chemotherapy treatments [33]. Thus, exploring alternative treatment strategies such as NTAPP becomes imperative. Our findings demonstrate that PTS treatment induced apoptosis in fibrosarcoma and head and neck cancer cells by elevating intracellular ROS levels and inducing mitochondrial dysfunction, while exhibiting no significant difference in apoptosis rates between PTS-treated and non-treated normal cells.

PTS treatment facilitated the generation of various radicals from three carrier gases; however, these radicals influenced cells through distinct mechanisms (Fig. S1d–f). Measurement of angular and radial radical generation revealed that helium/oxygen-based plasma produced substantially more hydrogen peroxide compared to nitrogen or argon/nitrogen-based plasma. This observation suggests that ROS derived from helium/oxygen-based plasma can impact cellular redox metabolism. Notably, treatment with NAC significantly restored cellular viability and suppressed apoptosis in cancer cells, providing compelling evidence for the close association between increased intracellular ROS levels and PTS-induced apoptosis.

Additionally, our study underscores the pivotal role of NRF2 in cellular responses to PTS-induced ROS stress. Under normal conditions, NRF2 is sequestered in the cytosol by Keap1 and targeted for proteasomal degradation. However, during oxidative stress, it is released from Keap1, translocates into the nucleus, and functions as a transcription factor to activate genes involved in antioxidant responses [34]. Previous studies have reported plasma-induced effects on NRF2 signaling in various cancer cells, including melanoma and non-small-cell lung cancer [10, 35]. Our results demonstrate increased NRF2 expression at both mRNA and protein levels in plasma-treated NF and HaCaT cells, coupled with heightened NRF2 translocation into the nucleus following PTS treatment. This observation suggests that the upregulation of antioxidant activity mediated by NRF2 plays a vital role in safeguarding normal cells against PTS-induced ROS stress.

p62 serves as a mediator in the crosstalk between autophagy and the Keap1-NRF2 pathway [36]. In this canonical pathway, oligomerized p62 undergoes phosphorylation, enhancing its binding affinity to polyubiquitinated cargo and Keap1. This process results in the release of NRF2 from Keap1, enabling its activation of several target genes, including p62, thus forming a feedback loop in the p62-Keap1-NRF2 axis. Ultimately, the polyubiquitinated cargo complex of p62 and Keap1 is degraded via autophagy [37, 38]. Our study reveals increased autophagy in PTS-treated normal cells, indicating that PTS activates the p62-Keap1-NRF2 pathway,

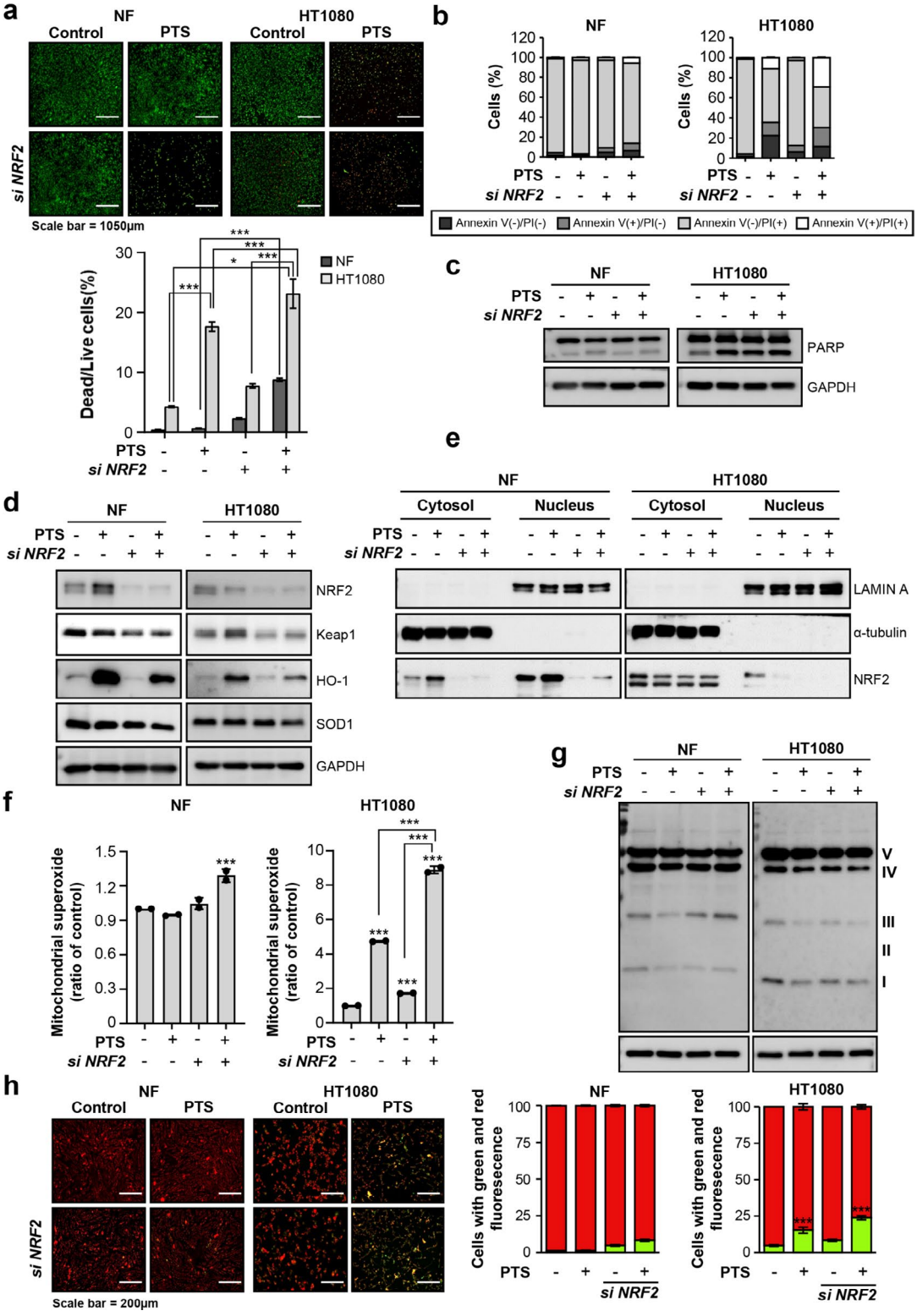

Fig. 5 Role of NRF2 in modulating reactive oxygen species (ROS)-dependent mitochondrial metabolic responses. NF and HT1080 cells were transfected with either siRNA targeting NRF2 or control siRNA and subsequently treated with PTS for 24 h. (**a**) Dead/live cell assay. Scale bar: 1050 μm. (**b**) Annexin V-propidium iodide staining. (**c**) Western blot analysis employing antibodies against PARP. (**d**) Western blot analysis utilizing antibodies against NRF2, Keap1, HO-1, and SOD1. (**e**) NRF2 localization in the cytoplasm and nucleus as determined by western blot analysis. (**f**) Measurement of mitochondrial superoxide levels. (**g**) OXPHOS complex levels determined by western blot analysis. (**h**) Measurement of mitochondrial membrane potential using JC-1 staining. Scale bar: 200 μm. $^{*}p < 0.05$; $^{***}p < 0.001$

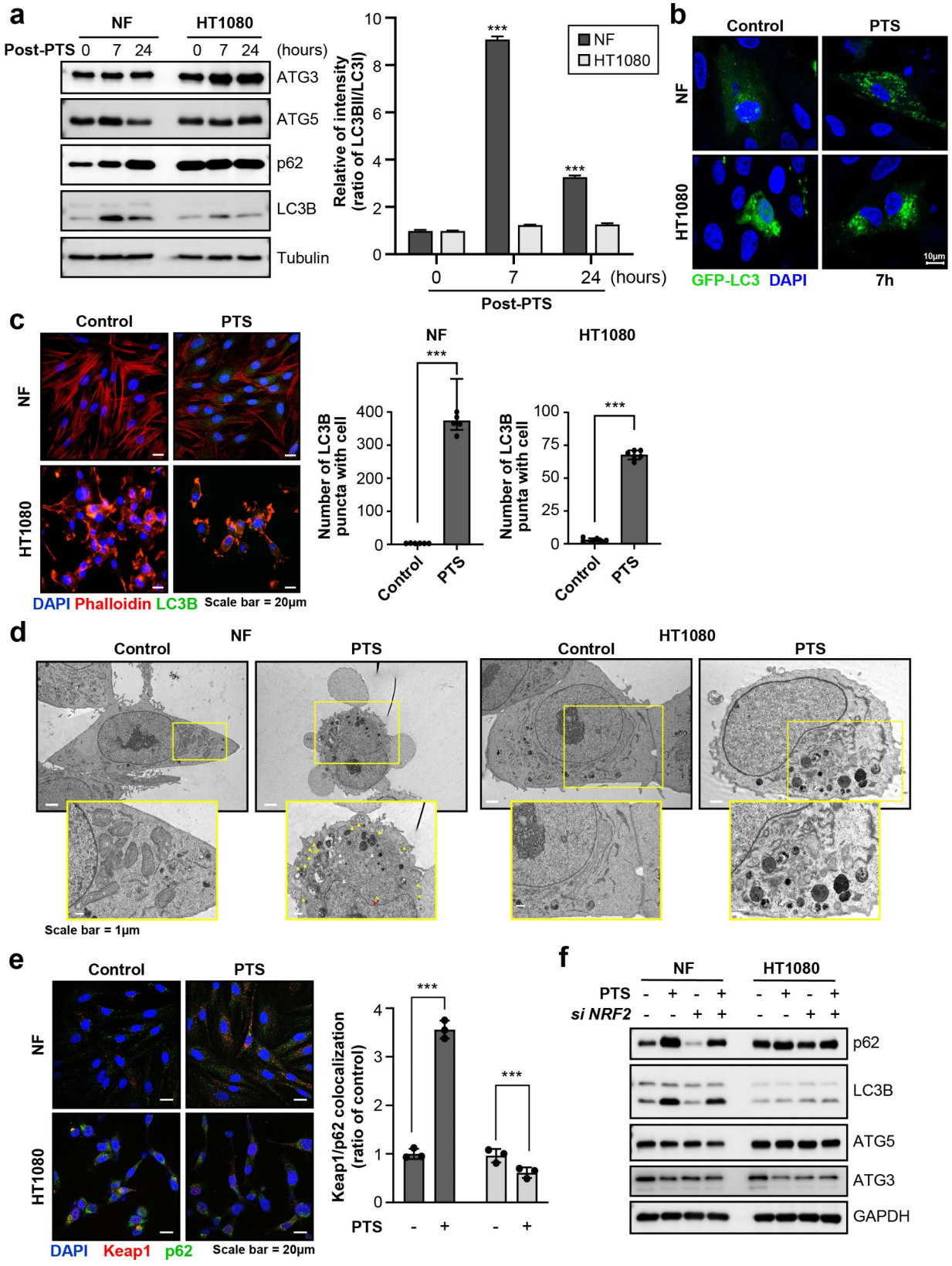

Fig. 6 (See legend on next page.)

(See figure on previous page.)

Fig. 6 Autophagy-mediated redox homeostasis maintenance via STSQM1/Keap1 interaction. (**a**) Western blot analysis results employing antibodies against autophagy-specific markers ATG3, ATG5, p62 and LC3B at 7- and 24-hours post-plasma-treated solution (PTS) treatment. The LC3II/LC3I ratio was measured. (**b**) Microscopic observation of GFP-LC3-transfected NF and HT1080 cells before and after PTS treatment (green: GFP-LC3; blue: DAPI). Scale bar: 10 μm. (**c**) LC3B immunofluorescence staining images of NF and HT1080 cells (blue: 4′,6-diamidino-2-phenylindole (DAPI); red: Phalloidin; green: LC3B). Scale bar: 20 μm. (**d**) Observation of PTS-induced autophagosome formation in NF and HT1080 cells via transmission electron microscopy. Scale bar: 1 μm. (**e**) Immunofluorescence staining images displaying Keap1 and p62 co-localization (blue: DAPI; red: Keap1; green: p62). Scale bar: 20 μm. (**f**) Western blot analysis outcomes employing antibodies against p62, LC3B, and Keap1 following treatment with PTS and NRF2 targeting siRNA. ***$p < 0.001$

and highly activated autophagy plays a protective role against oxidative stress in normal cells. However, contrary to the general understanding that p62 decreases during autophagy, our experiment showed an increase in p62. This could be interpreted as being related to NRF2 signaling. Overexpression of NRF2 induced by plasma may contribute to the accumulation of p62, one of target genes of NRF2.

While previous studies have reported the apoptotic effect of NTAPP on cancer cells, our study significantly advances the field of cancer therapy by uncovering underlying mechanisms associated with this effect. This study marks the first comparison of the distinct effects of plasma on fibrosarcoma and normal cells. We have confirmed that PTS promotes selective cell death in fibrosarcoma by downregulating the NRF2-induced ROS scavenger system, while PTS-treated normal cells exhibit survival through redox adaptation and activation of the ROS scavenger system. Furthermore, our findings indicate that PTS induces autophagy in normal cells to counteract oxidative stress. Although additional experiments are required to determine the optimal frequency and dosage of PTS administration, this study suggests the potential clinical application of PTS as a cancer treatment.

Abbreviations

NTAPP	Non-Thermal Atmospheric Pressure Plasma
ROS	Reactive Oxygen Species
NF	Normal Fibroblasts
PTS	Plasma-Treated Solution
NAC	N-Acetylcysteine
FACS	Fluorescence-Activated Cell Sorting
TUNEL	Terminal deoxynucleotidyl Transferase dUTP Nick End Labeling
RIPA	Radioimmunoprecipitation Assay
MMP	Mitochondrial Membrane Potential
GO	Gene Ontology
NGS	Next Generation Sequencing
NSP	Non-Side Population
SP	Side Population
TEM	Transmission Electron Microscopy
PARP	Poly ADP-Ribose Polymerase
LC3B	Microtubule-associated Proteins 1 A/1B Light Chain 3B
KHIDI	Korea Health Industry Development Institute
NRF	National Research Foundation of Korea
MOE	Ministry of Environment, Republic of Korea
EGCG	(-)-Epigallocatechin Gallate
BBA	Biochimica et Biophysica Acta
HT1080	Human Fibrosarcoma Cell Line
DAPI	4′,6-Diamidino-2-Phenylindole

Supplementary Information

The online version contains supplementary material available at https://doi.org/10.1186/s12964-024-01810-8.

Supplementary Material 1

Supplementary Material 2

Supplementary Material 3

Supplementary Material 4

Supplementary Material 5

Supplementary Material 6

Supplementary Material 7

Acknowledgements
We would like to thank Editage (www.editage.co.kr) for English language editing.

Author contributions
J.H.Y. analyzed the data and contributed to writing the manuscript; Y.H.Y. designed the study, contributed to writing the manuscript; C.H.H. designed the study, analyzed the plasma apparatus, wrote the manuscript, and conducted western blot analysis; S.U.K. designed the study, conducted the experiments, and contributed to writing the manuscript; C-H.K. supervised the experiments and contributed to writing the manuscript.

Funding
This work received support from the Korea Health Technology R&D Project through the Korea Health Industry Development Institute (KHIDI), funded by the Ministry of Health & Welfare, Republic of Korea [grant number HR21C1003]. It also received funding from the Basic Science Research Program through the National Research Foundation of Korea (NRF), funded by the Ministry of Science, ICT, and Future Planning [grant number RS-2023-00273483 to S.U.K], the Ministry of Environment (MOE) of Republic of Korea [grant number 2021003350001], and the Korea Health Technology R&D Project through the Korea Health Industry Development Institute (KHIDI) of Republic of Korea [grant number: RS-2024-00438448].

Data availability
All data generated or analyzed during this study are included in this published article and its supplementary information files.

Declarations

Ethics approval and consent to participate
Not applicable.

Consent for publication
Not applicable.

Competing interests
The authors declare no competing interests.

Received: 25 March 2024 / Accepted: 29 August 2024
Published online: 26 September 2024

References

1. Sung H, Ferlay J, Siegel RL, Laversanne M, Soerjomataram I, Jemal A, Bray F. Global cancer statistics 2020: GLOBOCAN estimates of incidence and

mortality worldwide for 36 cancers in 185 countries. CA Cancer J Clin. 2021;71:209–49.
2. Wang K-L, Yu Y-C, Chen H-Y, Chiang Y-F, Ali M, Shieh T-M, Hsia S-M. Recent advances in Glycyrrhiza glabra (Licorice)-Containing herbs alleviating radiotherapy-and chemotherapy-induced adverse reactions in cancer treatment. Metabolites. 2022;12:535.
3. Rébé C, Ghiringhelli F. Cytotoxic effects of chemotherapy on cancer and immune cells: how can it be modulated to generate novel therapeutic strategies? Future Oncol. 2015;11:2645–54.
4. Kong MG, Kroesen G, Morfill G, Nosenko T, Shimizu T, Van Dijk J, Zimmermann J. Plasma medicine: an introductory review. New J Phys. 2009;11:115012.
5. Metelmann H-R, Von Woedtke T, Weltmann K-D. Comprehensive clinical plasma medicine: cold physical plasma for medical application. Springer; 2018.
6. Kim S, Kim CH. Applications of plasma-activated liquid in the Medical Field. Biomedicines 2021, 9.
7. Kang SU, Kim YS, Kim YE, Park JK, Lee YS, Kang HY, Jang JW, Ryeo JB, Lee Y, Shin YS, Kim CH. Opposite effects of non-thermal plasma on cell migration and collagen production in keloid and normal fibroblasts. PLoS ONE. 2017;12:e0187978.
8. Sohbatzadeh F, Hosseinzadeh Colagar A, Mirzanejhad S, Mahmodi S. E. Coli, P. Aeruginosa, and B. cereus bacteria sterilization using afterglow of non-thermal plasma at atmospheric pressure. Appl Biochem Biotechnol. 2010;160:1978–84.
9. Yang X, Sun K, Zhu W, Li Y, Pan J. Time-dependent efficacy and safety of tooth bleaching with cold plasma and H2O2 gel. BMC Oral Health. 2022;22:1–9.
10. Ma J, Yu K, Cheng C, Ni G, Shen J, Han W. Targeting Nrf2-mediated heme oxygenase-1 enhances non-thermal plasma-induced cell death in non-small-cell lung cancer A549 cells. Arch Biochem Biophys. 2018;658:54–65.
11. Lin L, Wang L, Liu Y, Xu C, Tu Y, Zhou J. Non–thermal plasma inhibits tumor growth and proliferation and enhances the sensitivity to radiation in vitro and in vivo. Oncol Rep. 2018;40:3405–15.
12. Nima G, Harth-Chu E, Hiers RD, Pecorari VGA, Dyer DW, Khajotia SS, Giannini M, Florez FLE. Antibacterial efficacy of non-thermal atmospheric plasma against Streptococcus mutans biofilm grown on the surfaces of restorative resin composites. Sci Rep. 2021;11:23800.
13. Singh R, Manna P. Reactive oxygen species in cancer progression and its role in therapeutics. Explor Med. 2022;3:43–57.
14. Sarmiento-Salinas FL, Perez-Gonzalez A, Acosta-Casique A, Ix-Ballote A, Diaz A, Treviño S, Rosas-Murrieta NH, Millán-Perez-Peña L, Maycotte P. Reactive oxygen species: role in carcinogenesis, cancer cell signaling and tumor progression. Life Sci. 2021;284:119942.
15. National Academies of Sciences E, Medicine. Plasma science: Enabling Technology, sustainability, security, and Exploration. Washington, DC: National Academies; 2021.
16. Stryczewska HD, Boiko O. Applications of plasma produced with electrical discharges in gases for agriculture and biomedicine. Appl Sci (Basel). 2022;12:4405.
17. Kim SY, Kim HJ, Kang SU, Kim YE, Park JK, Shin YS, Kim YS, Lee K, Kim CH. Non-thermal plasma induces AKT degradation through turn-on the MUL1 E3 ligase in head and neck cancer. Oncotarget. 2015;6:33382–96.
18. Kang SU, Cho JH, Chang JW, Shin YS, Kim KI, Park JK, Yang SS, Lee JS, Moon E, Lee K, Kim CH. Nonthermal plasma induces head and neck cancer cell death: the potential involvement of mitogen-activated protein kinase-dependent mitochondrial reactive oxygen species. Cell Death Dis. 2014;5:e1056.
19. Park JK, Kim YS, Kang SU, Lee YS, Won HR, Kim CH. Nonthermal atmospheric plasma enhances myoblast differentiation by eliciting STAT3 phosphorylation. Faseb j. 2019;33:4097–106.
20. Chang JW, Kang SU, Choi JW, Shin YS, Baek SJ, Lee S-H, Kim C-H. Tolfenamic acid induces apoptosis and growth inhibition in anaplastic thyroid cancer: involvement of nonsteroidal anti-inflammatory drug-activated gene-1 expression and intracellular reactive oxygen species generation. Free Radic Biol Med. 2014;67:115–30.
21. Kang SU, Kim DH, Lee YS, Huang M, Byeon HK, Lee S-H, Baek SJ, Kim C-H. DIM-C-pPhtBu induces lysosomal dysfunction and unfolded protein response-mediated cell death via excessive mitophagy. Cancer Lett. 2021;504:23–36.
22. Shin YS, Kang SU, Park JK, Kim YE, Kim YS, Baek SJ, Lee S-H, Kim C-H. Anti-cancer effect of (-)-epigallocatechin-3-gallate (EGCG) in head and neck cancer through repression of transactivation and enhanced degradation of β-catenin. Phytomedicine. 2016;23:1344–55.
23. Klionsky DJ, Abdel-Aziz AK, Abdelfatah S, Abdellatif M, Abdoli A, Abel S, Abeliovich H, Abildgaard MH, Abudu YP, Acevedo-Arozena A et al. Guidelines for the use and interpretation of assays for monitoring autophagy (4th edition) (1). Autophagy 2021;17:1-382.
24. Kabeya Y, Mizushima N, Ueno T, Yamamoto A, Kirisako T, Noda T, Kominami E, Ohsumi Y, Yoshimori T. LC3, a mammalian homologue of yeast Apg8p, is localized in autophagosome membranes after processing. Embo j. 2000;19:5720–8.
25. Liou G-Y, Storz P. Reactive oxygen species in cancer. Free Radic Res. 2010;44:479–96.
26. Hayes JD, Dinkova-Kostova AT, Tew KD. Oxidative stress in cancer. Cancer Cell. 2020;38:167–97.
27. Bellezza I, Giambanco I, Minelli A, Donato R. Nrf2-Keap1 signaling in oxidative and reductive stress. Biochim et Biophys Acta (BBA)-Molecular Cell Res. 2018;1865:721–33.
28. Gañán-Gómez I, Wei Y, Yang H, Boyano-Adánez MC, García-Manero G. Oncogenic functions of the transcription factor Nrf2. Free Radic Biol Med. 2013;65:750–64.
29. Theodore M, Kawai Y, Yang J, Kleshchenko Y, Reddy SP, Villalta F, Arinze IJ. Multiple nuclear localization signals function in the nuclear import of the transcription factor Nrf2. J Biol Chem. 2008;283:8984–94.
30. Kasai S, Shimizu S, Tatara Y, Mimura J, Itoh K. Regulation of Nrf2 by mitochondrial reactive oxygen species in physiology and pathology. Biomolecules. 2020;10:320.
31. Chae SW, Choi G, Kim WJ, Lee ES, Shin SH, Park JH, Choi JW. Treatment results of soft tissue sarcomas in the head and neck. Head Neck. 1998;41:1454–8.
32. Aljabab AS, Nason RW, Kazi R, Pathak KA. Head and neck soft tissue sarcoma. Indian J Surg Oncol. 2011;2:286–90.
33. Augsburger D, Nelson PJ, Kalinski T, Udelnow A, Knösel T, Hofstetter M, Qin JW, Wang Y, Gupta AS, Bonifatius S. Current diagnostics and treatment of fibrosarcoma–perspectives for future therapeutic targets and strategies. Oncotarget. 2017;8:104638.
34. Jaramillo MC, Zhang DD. The emerging role of the Nrf2–Keap1 signaling pathway in cancer. Genes Dev. 2013;27:2179–91.
35. De Backer J, Lin A, Berghe WV, Bogaerts A, Hoogewijs D. Cytoglobin inhibits non-thermal plasma-induced apoptosis in melanoma cells through regulation of the NRF2-mediated antioxidant response. Redox Biol. 2022;55:102399.
36. Jiang T, Harder B, De La Vega MR, Wong PK, Chapman E, Zhang DD. p62 links autophagy and Nrf2 signaling. Free Radic Biol Med. 2015;88:199–204.
37. Katsuragi Y, Ichimura Y, Komatsu M. Regulation of the Keap1–Nrf2 pathway by p62/SQSTM1. Curr Opin Toxicol. 2016;1:54–61.
38. Dodson M, Redmann M, Rajasekaran NS, Darley-Usmar V, Zhang J. KEAP1–NRF2 signalling and autophagy in protection against oxidative and reductive proteotoxicity. Biochem J. 2015;469:347–55.

Publisher's note

Springer Nature remains neutral with regard to jurisdictional claims in published maps and institutional affiliations.